P. G. Allison
US Army Engineer Research & Development Center (ERDC), Vicksburg, MS 39081;
Department of Mechanical Engineering, Mississippi State University, Mississippi State, MS 39762

H. Grewal
Department of Mechanical Engineering, Mississippi State University, Mississippi State, MS 39762

Y. Hammi
Center for Advanced Vehicular Systems (CAVS), Mississippi State University, Mississippi State, MS 39762

H. R. Brown

W. R. Whittington

M. F. Horstemeyer

Department of Mechanical Engineering, Mississippi State University, Mississippi State, MS 39762

Plasticity and Fracture Modeling/Experimental Study of a Porous Metal Under Various Strain Rates, Temperatures, and Stress States

A microstructure-based internal state variable (ISV) plasticity-damage model was used to model the mechanical behavior of a porous FC-0205 steel alloy that was procured via a powder metal (PM) process. Because the porosity was very high and the nearest neighbor distance (NND) for the pores was close, a new pore coalescence ISV equation was introduced that allows for enhanced pore growth from the concentrated pores. This coalescence equation effectively includes the local stress interaction within the interpore ligament distance between pores and is physically motivated with these highly porous powder metals. Monotonic tension, compression, and torsion tests were performed at various porosity levels and temperatures to obtain the set of plasticity and damage constants required for model calibration. Once the model calibration was achieved, then tension tests on two different notch radii Bridgman specimens were undertaken to study the damage-triaxiality dependence for model validation. Fracture surface analysis was performed using scanning electron microscopy (SEM) to quantify the pore sizes of the different specimens. The validated model was then used to predict the component performance of an automotive PM bearing cap. Although the microstructure-sensitive ISV model has been employed for this particular FC-0205 steel, the model is general enough to be applied to other metal alloys as well. [DOI: 10.1115/1.4025292]

1 Introduction

Computational and mathematical based modeling of the thermomechanical behavior for powder metallurgy (PM) component design and performance prediction are recognized as significant contributions to improving efficiency, quality, and cost of current production and generating new business opportunities for the automotive industry. PM techniques are being incorporated to manufacture various complex shaped engineering components, which prove difficult to cast or shape by alternative procedures. A motivating factor driving the development of a mathematical based model is the ability to accurately predict the variation in property performance caused by inhomogeneous density distribution. Research addressing mathematical modeling will provide several benefits including: near net shape components, complex geometries, high strength and minimal or eliminated finishing operations [1].

In this paper, we address stress-state dependence and associated material modeling to capture the different yield stress, work hardening, and failure strain effects in a very porous metal alloy. Although some porous plasticity models have been employed in the past (cf. [2–9]) based on pore volume fractions, none of these formalisms included microstructural features such as nearest neighbor distance of pores, grain size effects, stress state dependence, particle size effects, particle volume fraction effects, and temperature and strain rate dependence on each of the void nucleation and coalescence equations. The physics-based model that includes microstructure-based internal state variables for plasticity and damage based upon Bammann [10–14], and later improved by Horstemeyer and Gokhale [15] and Horstemeyer et al. [8] by including pore nucleation, pore growth, and pore coalescence evolution equations is used to correlate to the experimental data. The McClintock [16] pore growth rule is used for pores growing from particles, while the Cocks and Ashby [17] pore growth rule is applied for pre-existing pores growing. In this paper, we present all of the pertinent structure-property experiments along with the model calibration and model validation results showing the robustness of the model over various temperature, stress state, and strain rate excursions.

2 Microstructure-Based ISV Plasticity-Damage Model

A physically-based model including microstructure-based internal state variables for plasticity and damage based on the work of Bammann [10–14], Horstemeyer and Gokhale [15], and Horstemeyer et al. [8] was used as a basic framework for this very porous metal study. The McClintock pore growth rule was incorporated for pores growing from particles [16], while the Cocks and Ashby's pore growth rule was used for pre-existing pore growth [17]. All of the associated equations are shown in Appendix A, but the main differing equations are illustrated here in the text to elucidate our contribution.

The multiplicative decomposition of the deformation gradient into elastic and plastic parts is assumed. The deformation gradient, $\underline{F}$, connects a point in the reference (nondeformed) configuration to the same point in the current (deformed)

Contributed by the Materials Division of ASME for publication in the JOURNAL OF ENGINEERING MATERIALS AND TECHNOLOGY. Manuscript received December 29, 2011; final manuscript received August 1, 2013; published online September 19, 2013. Editor: Hussein Zbib.

This material is declared a work of the US Government and is not subject to copyright protection in the United States. Approved for public release; distribution is unlimited.

Copyright © 2013 by ASME

Downloaded From: http://materialstechnology.asmedigitalcollection.asme.org/ on 09/25/2013 Terms of Use: http://asme.org/terms

configuration. Work by Lee [18] showed that the decomposition of the deformation gradient, $\underline{F}$, into elastic, $\underline{F}^e$, and plastic, $\underline{F}^p$, parts as Eq. (1).

$$\underline{F} = \underline{F}^e \underline{F}^p \tag{1}$$

Here, the elastic deformation gradient, $\underline{F}^e$, represents the reversible elastic stretching and rotation of the crystal lattice in the current (deformed) configuration. The plastic deformation gradient, $\underline{F}^p$, describes the irreversible plastic deformation due to crystallographic slip. The addition of volumetric changes on the multiplicative decomposition was described by Bammann and Aifantis [11] based on Lee's work [18]. Here, the plastic deformation gradient splits into an isochoric inelastic, $\underline{F}^p_d$, and a volumetric inelastic, $\underline{F}^p_v$, part. The multiplicative decomposition of the deformation gradient is given by

$$\underline{F} = \underline{F}^e \, \underline{F}^p_d \, \underline{F}^p_v \tag{2}$$

The Jacobian of the volumetric plastic deformation gradient in Eq. (2) characterizes the change in volume or change in density due to pores nucleating and growing for a constant mass.

$$J = \det(\underline{F}^p_v) = \frac{V_1}{V_0} = \frac{\rho_0}{\rho_1} \tag{3}$$

Assuming that the volume in State 0 and State 1 are equal due to inelastic incompressibility, then the change in volume from State 0 (reference configuration) to State 1 (intermediate configuration) is

$$V_1 = V_0 + V_v \tag{4}$$

where V_1 and ρ_1 are the volume and density in State 1, respectively. Then, V_0 and ρ_0 are the volume and density in State 0, respectively. The term V_v is a new term added from the volume of the pores. From Eq. (3), damage, φ, is defined as the ratio of volume in elastically unloaded State from the reference volume to the volume in the intermediate configuration

$$\varphi = \frac{V_1 - V_0}{V_1} = \frac{V_v}{V_1} \tag{5}$$

In the context of this kinematic framework, the evolution of damage given by Horstemeyer [19] is

$$\varphi = (\eta\nu + \varphi_{\text{pore}})c \tag{6}$$

where c is a coalescence term, η is a pore nucleation term, ν is a pore growth term, and φ_{pore} is the damage originating from preexisting pores. The nucleation term, η, is the number of pores per unit volume with Horstemeyer [19] expressing the term in rate form as

$$\dot{\eta} = \dot{\varepsilon}\left(\frac{d^{0.5}}{K_{\text{IC}} f^{1/3}}\eta\left\{a\left[\frac{4}{27} - \frac{J_3^2}{J_2^3}\right] + b\frac{J_3}{J_2^{3/2}} + c_2\left\|\frac{I_1}{\sqrt{J_2}}\right\|\right\}\right)\exp\frac{C_{T\eta}}{T} \tag{7}$$

where $\dot{\varepsilon}$ is the strain rate, d is the average inclusion particle size, K_{IC} is the fracture toughness, f is the initial pore volume fraction, a, b, c_2, and $C_{T\eta}$ are material constants, J_2 and J_3 are the second and third deviatoric stress invariants, I_1 is the first invariant of stress. The pore growth equation currently used is from McClintock [16]

$$\dot{\nu} = \frac{4}{3}\left[R_0 \exp\left(\dot{\varepsilon}\frac{\sqrt{3}}{2(1-n)}\right)\sinh\left(\sqrt{3}(1-n)\frac{\sqrt{2}I_1}{3\sqrt{J_2}}\right)\right]^3 \tag{8}$$

where R_0 is the initial pore radius and n is the strain-hardening exponent. The damage originating from the initial pores in the material is from Cocks and Ashby [17]

$$\dot{\varphi}_{\text{pores}} = \left[\frac{1}{(1-\varphi_{\text{pores}})V(T)/Y(T)} - (1-\varphi_{\text{pores}})\right] \times \sinh\left\{\frac{2(2m-1)}{2m+1}\frac{\sigma_h}{\sigma_e}\right\}\|\dot{\varepsilon}\| \tag{9}$$

where m is a material constant, σ_h and σ_e are the hydrostatic and equivalent Von Mises stresses, respectively.

A new coalescence equation is based on previous work by Horstemeyer [20] where coalescence effects were studied as a function of temperature and pore arrangement in a matrix. The equation introduced here is a function of both pore size and pore spacing

$$\dot{C} = \left(\frac{4d_0}{\text{NND}}\right)^{\zeta}\exp(C_{\text{TC}}T)\dot{\varepsilon} \tag{10}$$

where T is the temperature, C_{TC} is the temperature dependent material constant, d_0 is the pore diameter, NND is the pore nearest neighbor distance, ε is the total strain, and ζ is a material constant. The coalescence Eq. (10) implements the micromechanical finite element results of Horstemeyer [20] in which the critical distance between pores resulting in maximum coalescence was four pore diameters between pores; this equation is also the first to include a microstructural feature such as the nearest neighbor distance of pores. The coalescence equation is illustrated by a nonlinear behavior as observed in Fig. 1 where the effect d_0 has on coalescence is depicted. Hence, Eqs. (6), (7), and (10) are different equations than those found in the literature in that they reflect microstructural measurable content within the rate equations. So evolution equations for damage nucleation, growth, and coalescence evolve differently under varying stress states, temperatures, and strain rates.

The trend in Fig. 1 depicts that the coalescence increases more noticeably at higher plastic strain levels when the average pore diameter, d_0, increases. In other words, the distance between pores is so close that their associated stress fields affect each other such that the pores grow faster compared to the case if the neighboring pores were not present. A similar trend is observed in Fig. 2, which illustrates the effect of how increasing the material constant, ζ, adjusts the coalescence equation.

As the constant ζ increases, more nonlinearity is observed for the coalescence at higher plastic strain levels than lower values as observed in Fig. 2. A higher value of coalescence is also illustrated with an increasing ζ. The dependence of how decreasing (or

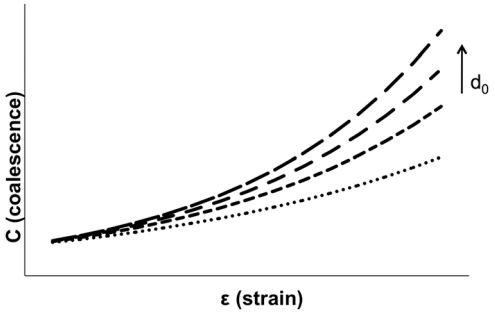

Fig. 1 Coalescence enhancement as a function of strain portraying how an increasing pore diameter increased the coalescence for pore growth

Downloaded From: http://materialstechnology.asmedigitalcollection.asme.org/ on 09/25/2013 Terms of Use: http://asme.org/terms

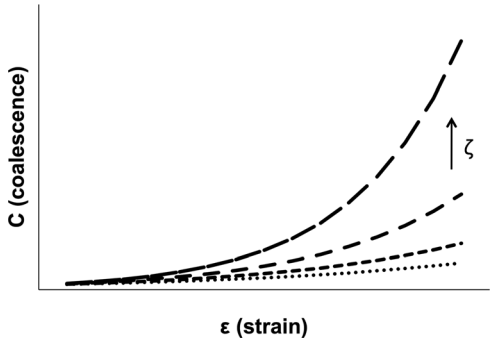

Fig. 2 Coalescence enhancement as a function of strain portraying how an increasing coalescence exponential, ζ, increased the coalescence for pore growth

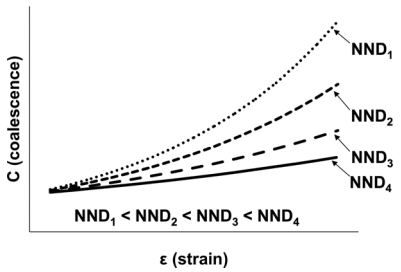

Fig. 3 Coalescence enhancement as a function of strain portraying how a decreasing pore nearest neighbor distance, NND, increased the coalescence for pore growth

increasing) the distance between pores adjusts the coalescence equation is clarified in Fig. 3.

The increase in pore spacing is depicted in Fig. 3 gives a reduction in coalescence. More nonlinearity and higher values of the coalescence equation curve are observed as the distance between pores decreased.

3 Model Set-Up and Calibration on FC-0205

The plasticity-damage model required calibration and validation before use in the design optimization process. To calibrate the model, a set of constants were determined that describe the model for a certain material. One set of constants was determined by using experimental true stress–strain data for different stress states, strain rates, and temperature effects. The other set of the constants were determined from the microstructural information of the experimental specimens and the open literature.

3.1 Material Composition. Water atomized iron powder, Atomet 1001, from Quebec metal powders was the base iron powder for the FC-0205 material used in the study. A nominal composition of 2 wt. % Cu, 0.05 wt. % graphite, and balance iron was blended, binder treated, pressed, and sintered into rectangular compacts with sintered densities of 6.35 g/cm^3 and 7.05 g/cm^3 via a proprietary process developed by Metaldyne, LLC [21].

3.2 Experimental Procedure. A series of compression, tension, and torsion experiments were performed to quantify the microstructure-property correlations for calibration of the internal state variable plasticity-damage model that admits heterogeneities of microstructures and defects. Tension and compression tests were performed on standard ASTM specimens machined from the sintered blanks. ASTM E8 hour-glass cylindrical specimens with a gage diameter of 6.35 mm and a gage length of 25.4 mm were used for tension testing [22]. Cylindrical compression specimens were machined with a diameter of 8.20 mm and a height of 9.84 mm. The torsion tests employed a Lindholm type specimen design with an outside diameter of 19.05 mm, an inside diameter of 9.53 mm, and a gage length of 2.08 mm.

Table 1 Damage parameters obtained from fracture surfaces of low and high porosity ambient (293 K) tensile specimens

	Low initial porosity specimens	High initial porosity specimens
$\varphi_{initial}$	0.09	0.19
	Observations of fracture surface	
d (μm)	32.03	27.41
$v{\cdot}c$ (μm^2)	806.72	591.38
η (#/μm^2)	0.0009	0.0015
$\varphi_{fracture}$	0.73	0.92

All tests were performed at a strain rate of 10^{-4}/s and at one room temperature of 293 K. Additionally, tension and compression tests were also performed at a temperature of 593 K.

High rate compression experiments were also performed on cylindrical specimens at 293 K to capture strain rate effects. All tests were performed on specimens machined from rectangular blanks compacted and sintered by Metaldyne, LLC at a sintered density of 6.35 g/cm^3 and 7.05 g/cm^3. A detailed explanation of the structure-property experimental procedure may be found in the publication by Allison et al. [23].

3.3 Description of the Model. As stated earlier, the plasticity-damage model required calibration and validation before use in the design optimization process. The material constants and microstructural quantities are provided in Appendices B and C, respectively. The fracture toughness, $K_{IC} = 40$ MPa$\sqrt{m}$ was obtained from the literature [24]. However, the averages for initial pore radius, pore volume fraction, initial particle size, particle volume fraction, and grain size were determined from microstructural analysis as discussed previously in the manuscript by Allison et al. [23]. From image analysis, we quantified the microstructural quantities and the damage parameters from examining the fracture surface of failed specimens and the data are reported in Table 1.

The damage parameters were obtained from fracture surface image analysis on a minimum of four SEM images for three specimens at different initial porosity levels. Specimens with lower initial porosity (approximately 9%, which really is not that low when compared to castings, extrusions, and rolled material but is relatively low when compared to the other PM specimens in this study) exhibited a larger average pore diameter, d, on the fracture surface than the higher initial porosity specimens. Because the higher initial porosity (approximately 19%) specimens had a greater pore density, the nucleation term, η, in Table 1 was greater for those specimens. No new pore nucleation occurred upon deformation as the energy dissipation incurred by pores growing upon deformation into each other fairly rapidly. Note from Table 1 that the specimens with less initial porosity exhibited more pore growth, v, and coalescence, c, on the fracture surfaces because they had a lower number of pores at the beginning.

DMGFIT, a fitting software developed at Mississippi State University (MSU) based on the ISV plasticity-damage model [8], was used for determining the plasticity and damage constants for the model. Figures 4–6 were all determined at one time with one set of plasticity-damage constants. Because the algorithm tried to optimize the whole set data and not just one curve, all of the curves were not exactly captured by the model; however, the model typically captured the main features within the uncertainty bands of the experimental data. Simultaneous fitting of the different curves (tension, compression, and torsion) are capable with the DMGFIT software as shown in Figs. 4 and 5, respectively.

Downloaded From: http://materialstechnology.asmedigitalcollection.asme.org/ on 09/25/2013 Terms of Use: http://asme.org/terms

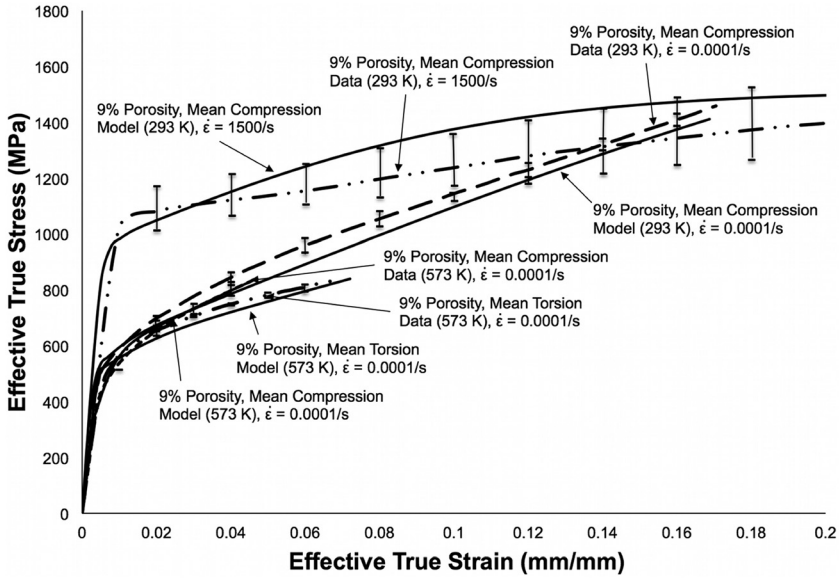

(a)

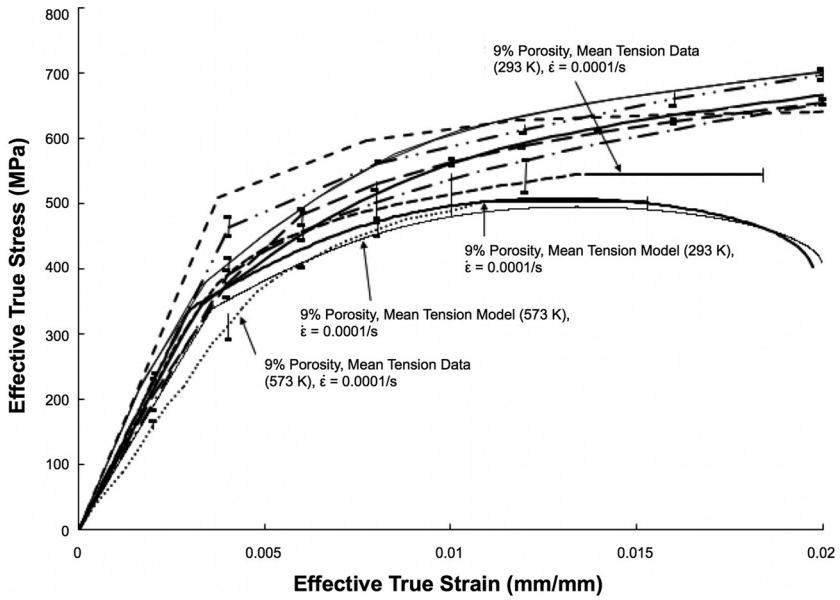

(b)

Fig. 4 Internal state variable plasticity-damage model calibration for mean monotonic stress–strain behavior under different stress states and temperatures with a relatively low initial porosity (9%); (*a*) shows long range transients of the stress–strain behavior up to 20% strain and (*b*) shows the short range transients up to 2% strain

The smooth lines in Figs. 4 and 5 are the model results, where the data points are averaged experimental data from experiments tested at different stress states, strain rates, and temperatures for the low porosity specimens in Fig. 4 and the high porosity specimens in Fig. 5. The hardening and recovery of the experimental data curves are correlated well by the model for low strain rate tests. Further fine-tuning of the model constants would allow for more accurate prediction of the high rate compression data. However, the model captured the elongation to failure of the tension specimens within the uncertainty of the experimental data. Finite element analyses using a single element also verified the model giving the same answers as the DMGFIT software, which is essentially a self-contained material point simulator.

The ambient tensile test data in Fig. 6 provides a mean data point curve from three high porosity experiments and three low porosity experiments. The upper bound and lower bound data curves both have an uncertainty band on the strain-to-failure in the figure.

The onset of yield is captured by the model even though the elastic modulus appears slightly lower than the experimental data. For the upper bound model curve, the modulus is plotted lower than the mean data and the lower bound model prediction plots the curve below or on the lower bound data (data shows that experiment is not linear all the way to where we are predicting yield.). The plastic hardening and recovery portions are captured by the model since the upper bound model is plotted between the

Downloaded From: http://materialstechnology.asmedigitalcollection.asme.org/ on 09/25/2013 Terms of Use: http://asme.org/terms

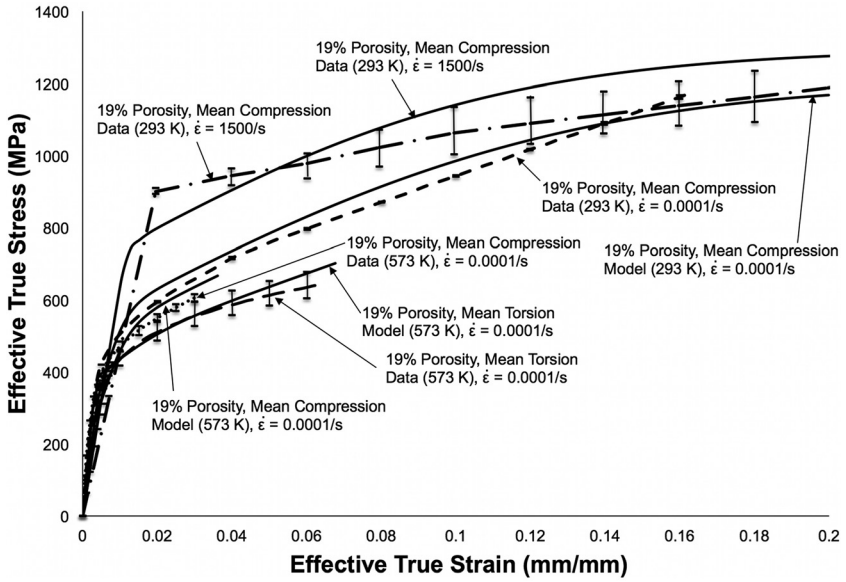

(a)

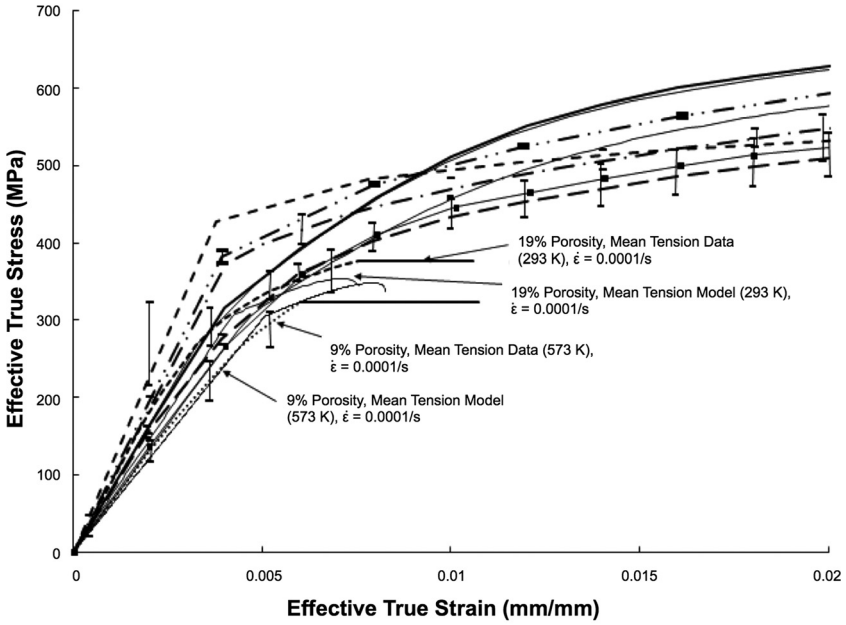

(b)

Fig. 5 Internal state variable plasticity-damage model calibration for mean monotonic stress–strain behavior under different stress states and temperatures with a high initial porosity (19%): (*a*) shows long range transients of the stress–strain behavior up to 20% strain and (*b*) shows the short range transients up to 2% strain

mean and upper bound data. The plasticity portion of the lower bound model is graphed between the lower bound data and the mean data points.

The damage evolution curves are plotted in Fig. 7 for both the 293 K and 573 K tensile experiments. Clearly, the damage model does a great job of capturing the elongations-to-failure thus giving confidence of the predictability capability of the model.

The damage evolution in Figs. 7(*a*) and 7(*b*) for the low initial porosity tensile specimens under predicts the damage evolution resulting in slightly larger strain-to-failures than what was observed experimentally. However, for the high initial porosity specimens the elongation-to-failure is within the uncertainty band of the experimental data for the two temperature levels.

4 Model Validation of FC-0205 Powder Metallurgy Steel

Once the material constants were determined from the calibration experiments, they no longer should be altered. Validation of the model occurred by comparing the plastic and damage behavior of the material with notch Bridgman tensile specimens [19] and the main bearing cap.

4.1 Notch Bridgman Tensile Testing Validation. The notch Bridgman [19,25] specimens allow for different stress triaxiality conditions to influence the damage progression differently. Two different notch radii were chosen for the analysis. The specimens

Downloaded From: http://materialstechnology.asmedigitalcollection.asme.org/ on 09/25/2013 Terms of Use: http://asme.org/terms

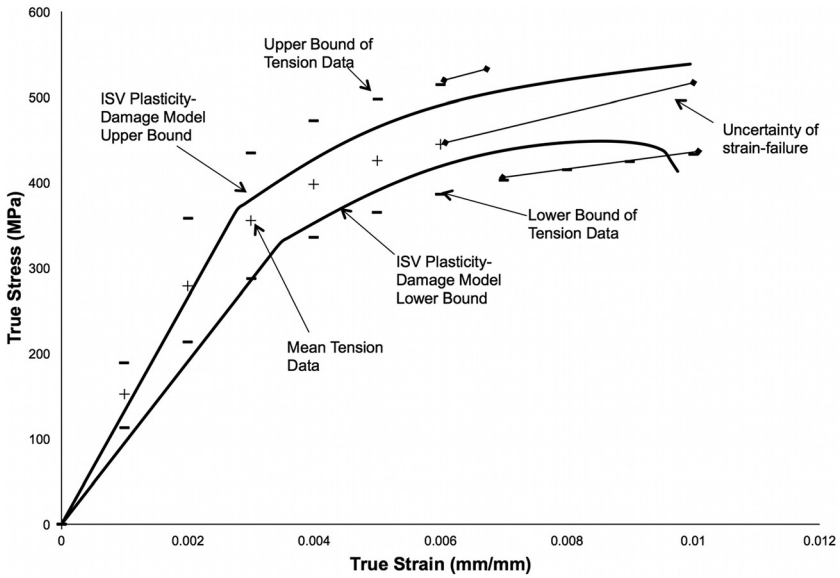

Fig. 6 Internal state variable plasticity-damage model calibration for mean monotonic tension experimental data with an initial relatively low porosity (9%) and high porosity (19%)

are labeled in this writing as R15 and R38 having a notch radii of $R = 0.15$ cm and $R = 0.38$ cm, respectively. The ratio between one half of the cross-sectional diameter of the specimen at the centre of the notch, a, respect to the notch radius, r. Therefore, R15 has a ratio $a/r = 0.142/0.06 = 2.367$ and for R38 the $a/r = 0.142/0.075 = 1.893$.

Monotonic loading of notch Bridgman specimens was performed up to and including failure. The use of the notch geometry created stress gradients in the specimens similar to structural components, allowing for experimental and numerical methods to be validated in preparation for the prediction of actual stress and damage in real engineering components.

Experiments on notch Bridgman specimens were performed to failure and then other specimens were tested to 98%, 95%, and 90% of the failure load using an Instron 5882 testing machine, with a ± 100 kN maximum loading capacity. Although the tests were run in strain control using an Instron 2630-052 extensometer at a strain rate of 0.0001/s in the unnotched region, the load was monitored to know when stoppage occurred.

Image analysis results of the microstructure showing pore characteristics of the notch tensile specimens are provided in Fig. 8. The pore diameter, nearest neighbor distance and porosity level data obtained from image analysis of optical micrographs of the notch specimens examined as in Fig. 8 is provided in Table 2 showing that the specimens had very close microstructural characteristics.

Fracture surfaces of the Bridgman specimens for both notch root radii are shown as SEM images in Fig. 9. SEM analysis of the Bridgman fracture surfaces depict the powder particles with cleaved and micropore fractures for both radii tested. The image analysis results of the fracture surfaces provided the damage information in Table 3. The results from these surfaces show that coalescence was the main source of damage growth, with some pore growth during deformation. The pore nucleation density essentially remained the same because with so many pores at the beginning, the easiest mechanism for dissipation was pore growth that was enhanced by coalescence. When comparing Tables 2 and 3 information, one can see that the total pore volume fraction grew from approximately 9–10% to 85–86% at fracture.

To validate the notch tensile tests and predict the location of failure, the notch specimen was modeled using the finite element method with the boundary conditions shown in Fig. 10. The notch specimen was modeled as a deformable body with Young's Modulus varying as a function of distributed density as defined in the user material subroutine UMAT with the use of C3D8R continuum brick elements. The notch specimen was subjected to displacement time loading in which the lowest cross-section in the notch region was fixed and the top part was subjected to loading as shown in Fig. 10.

Damage levels are nonlinearly related to the magnitude of the triaxiality [20]. Thus, larger levels of triaxiality will translate into greater regions where the pores grow and coalesce. To validate the accuracy of the plasticity-damage model, both the plasticity and damage progression were analysed using the finite element model for each of the notch specimens tested. As shown in Fig. 11, the contour plots of these results indicate that the central region in specimen has the highest level of triaxiality consistent with [20].

The load–displacement curves for the notch specimens were used to "validate" the plasticity of the model as the material constants were already fixed from the model correlation experiments and clearly the model follows the experimental trends as shown in Fig. 12. The model captures the maximum load and fracture displacement for the R15 and R38 specimens. The model load–displacement curves show a very slight variation in the elastic slope, while in the experiments the variation was more noticeable showing either variation in machine compliance or greater distributions in the specimen porosity. The model also captures satisfactorily the elongation path for the R15 and R38 notch specimens.

Figure 12 shows a good correlation between the experimental and finite element model results. The model predicts satisfactorily the damage location of the notch subjected to tensile loading, and a size effect where the larger radius exhibits more plasticity than the smaller radius specimens during testing. The stress triaxiality in the center of the notch region as shown in Fig. 10 causes the pores to grow and coalesce, which results in damage to be greater at the notch center. Furthermore, the finite element model predicts the same load–displacement curve as the experiment up to a maximum point where damage reaches a critical value.

4.2 Main Bearing Cap Validation. Once the material model has been calibrated and validated, then it can be used in the design

Downloaded From: http://materialstechnology.asmedigitalcollection.asme.org/ on 09/25/2013 Terms of Use: http://asme.org/terms

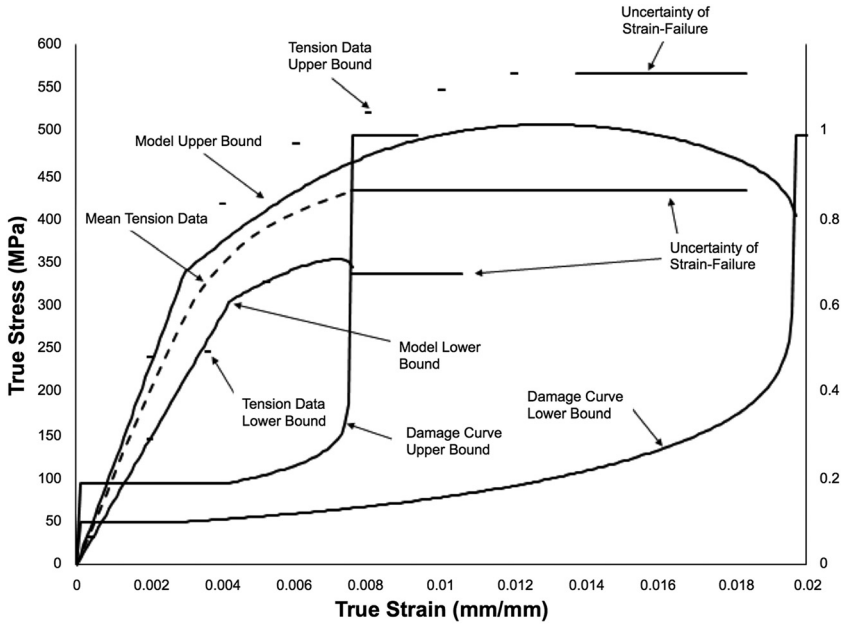

(a)

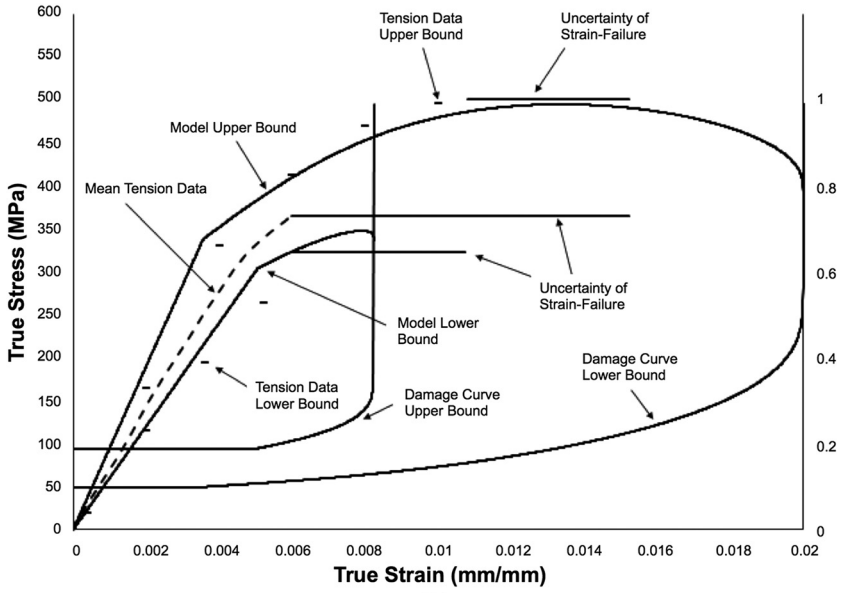

(b)

Fig. 7 Experimental and finite element model simulated stress–strain curves and the associated damage evolution for the uniaxial tension tests carried out at (*a*) 293 K and (*b*) 573 K

process to help predict behavior of structural components particularly pertaining to the durability and life of the components. These techniques are helpful in predicting the location of failure of the component, stress distributions, cracks initiating during the tensile or fatigue loading. However, for the material model to be accurate and successful, computer simulation should be accompanied with a complete experimental database for validation. In our case, these validation experiments included several test methods such as monotonic load testing and fatigue testing of the automotive main bearing cap.

Monotonic tension experiments were conducted on sintered main bearing caps (MBCs) at room temperature (~273 K) in laboratory air with relative humidity near 45–60 RH. The loading was applied on the legs of the MBC as shown by the arrows in Fig. 13.

Testing was conducted in displacement control at a rate of 0.25 mm/s. The MBCs were preloaded to 133 N, which ensured that the load was applied at the end of the bearing cap feet. A nut and bolt were used to set the loading location and also to ensure the surface of the MBC remained in the same plane as the finite element simulations employed the boundary condition. Data acquisition was recorded every 100 ms with the extension, load, and displacement recorded. The load–displacement curves of the MBCs from the monotonic tests are reported in Fig. 14, where the displacement is reported from the crosshead displacement of the load cell. The failure location was the same for all the MBCs tested.

The finite element mesh of the MBC loading setup included the MBC, which was modeled by the proposed ISV formulation

Downloaded From: http://materialstechnology.asmedigitalcollection.asme.org/ on 09/25/2013 Terms of Use: http://asme.org/terms

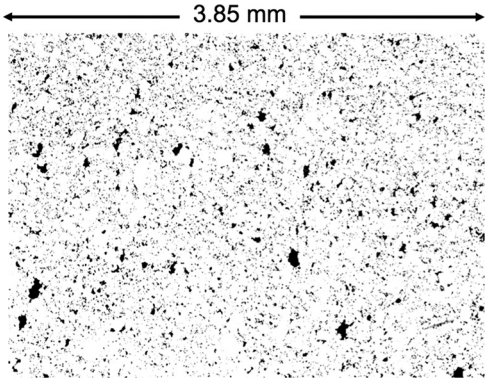

Fig. 8 Initial porosity optical micrograph of notch tensile specimens at 293 K for the relatively low porosity (9%) specimen

described in this effort, and two rods protruding through the bearing cap ends. The rods were meshed as a rigid body with R3D4 rigid elements, while the bearing cap was meshed using C3D8R continuum brick elements. Since rods were defined as the rigid bodies, they were not influenced by the forces and stresses acting on the model. Boundary conditions were applied to the rods, with loading applied to one rod while the other rod was fixed. As shown in Fig. 15(*a*), the porosity distribution of the MBC from the compaction computational results were used as input for the performance model. Because the density variation during sintering was very small (0.2–0.3%) for the FC-0205 iron-based powder, the density variation during sintering was not considered, so the density distribution was directly mapped from the compaction FE analysis after springback, using the feature *MAP SOLUTION in ABAQUS/Standard.

The mechanical properties of the MBC depended upon the heterogeneities of the porosity and grain size. The material model [8]

Table 2 Image analysis of the initial porosity optical micrographs for the notch tensile specimens

	Small notch root radius		Large notch root radius	
Low porosity image analysis	Average	Maximum	Average	Maximum
Pore diameter, d (μm)	8.34	130.13	8.31	149.04
NND (μm)	12.62	72.61	12.51	69.65
Porosity, φ	0.0972	—	0.0939	—
Pore nucleation density, η (#/μm^2)	0.00178	—	0.00173	—
Pore volume *coalescence, $v{\cdot}c$ (μm^2)	54.7	—	54.2	—

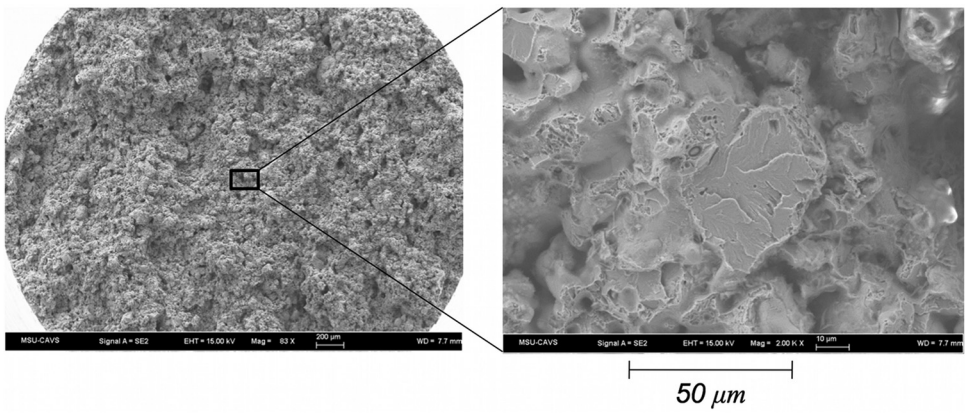

(a)

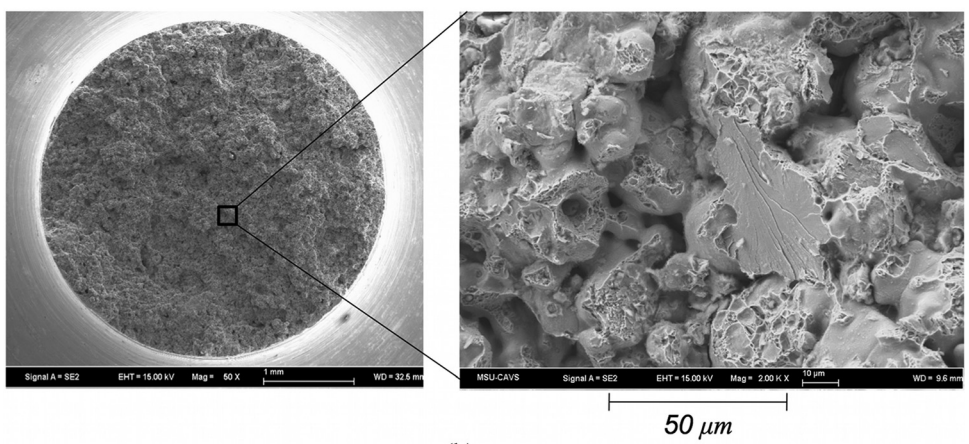

(b)

Fig. 9 SEM fracture surface images of Bridgman specimens with notch radii of (*a*) 0.38 cm and (*b*) 0.15 cm

Downloaded From: http://materialstechnology.asmedigitalcollection.asme.org/ on 09/25/2013 Terms of Use: http://asme.org/terms

Table 3 Damage parameters obtained from fracture surfaces of large and small notch root radii tensile specimens

	Large notch root radius	Small notch root radius
Pore diameter, d (μm)	24.58	21.64
Pore volume *coalescence, $v \cdot c$ (μm^2)	474.57	367.79
Pore nucleation density, η (#/μm^2)	0.0018	0.0023
Porosity, φ	0.86	0.85
NND (μm)	9.08	4.30

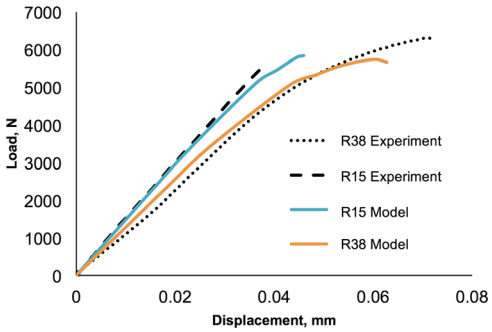

Fig. 12 Load–displacement comparison between the experimental results and the FEA results for notch tensile tests (R15 and R38 specimens)

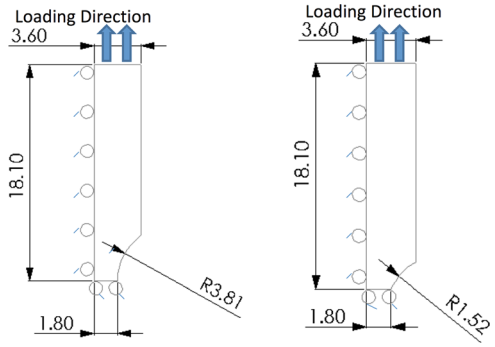

Fig. 10 Boundary conditions of the notch Bridgman specimens for finite element analysis with different states of stress triaxiality

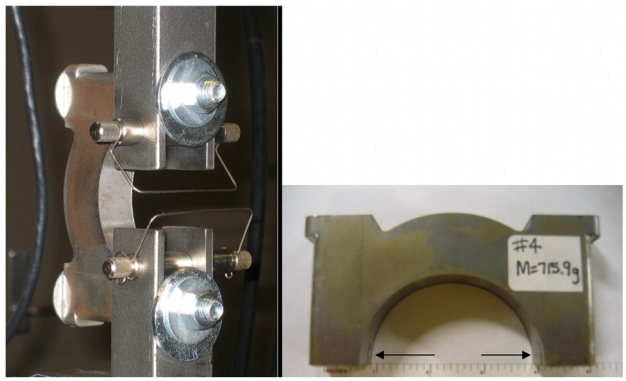

Fig. 13 Test fixture and loading application of the powder metal steel MBC

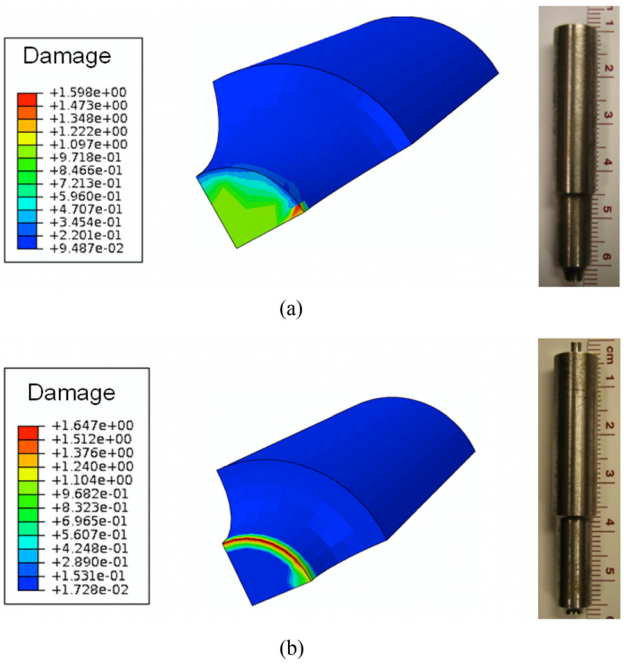

Fig. 11 Comparison of failure location for the (*a*) R38 and (*b*) R15 notch Bridgman tensile speciments with failure denoted by the damage parameter in the qaurter space finite element simulations

included damage dependent material parameters that include the direct measurements of the pore sizes, nearest neighbor distances of the pores, porosity, and grain size in order to capture the location of failure during monotonic loading. Figure 16 compares the monotonic testing of the MBC experiment to the finite element model results. Clearly, the performance model predicted the failure location at the same point where the experiment exhibited the behavior approximately 45 deg in the arch denoted by Region C in Fig. 16(*a*) that corelates to the fractured specimen in Fig. 16(*b*). Regions A and B as shown in Fig. 16(*a*) refer to the maximum Von Mises stress, which is not the region of crack initiation and maximum damage. The Von Mises stress is typically used to determine the "hot" spot on a component for failure. However, these simulations indicate that the Von Mises stress would have given the wrong location and thus should not be used for the criterion for crack initiation, because it does not take into account the heterogeneous porosity distribution in the bearing cap not does necessarily align with the greatest stress triaxiality.

Another part of the model validation was related to the measurement of strains in a region not necessarily near the fracture location. Strain gages were applied to the MBC as shown in Fig. 16(*b*). Figure 17 shows that the simulation strain versus displacement follows that of the experiment.

The comparison of the finite element simulations with the experimental results illustrates the excellent correlation between the model and tests. Now that the calibrated ISV plasticity-damage model was validated via the notch tensile specimens and the MBC, it can be used with confidence for design and analysis of powder metals and structural components.

Downloaded From: http://materialstechnology.asmedigitalcollection.asme.org/ on 09/25/2013 Terms of Use: http://asme.org/terms

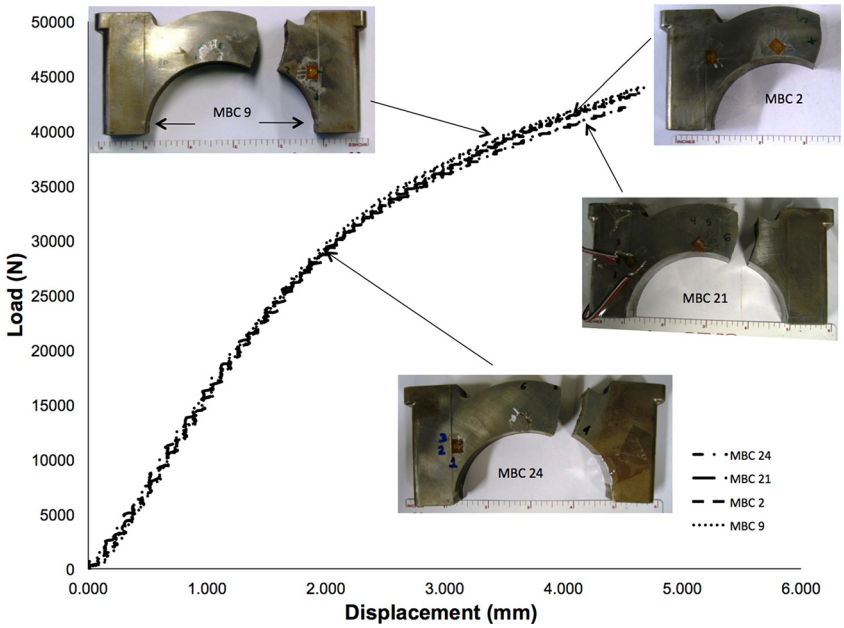

Fig. 14 Plot of load–displacement results for the main bearing caps

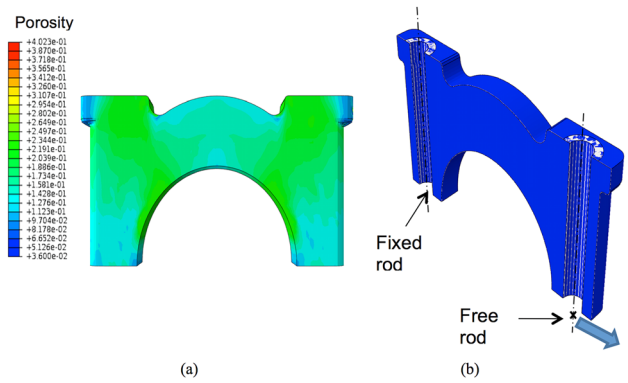

Fig. 15 Finite element model for monotonically loaded test showing (*a*) the initial porosity solution (SDV28) of the main bearing cap transferred from the compaction model results and (*b*) the performance model configuration with applied boundary conditions.

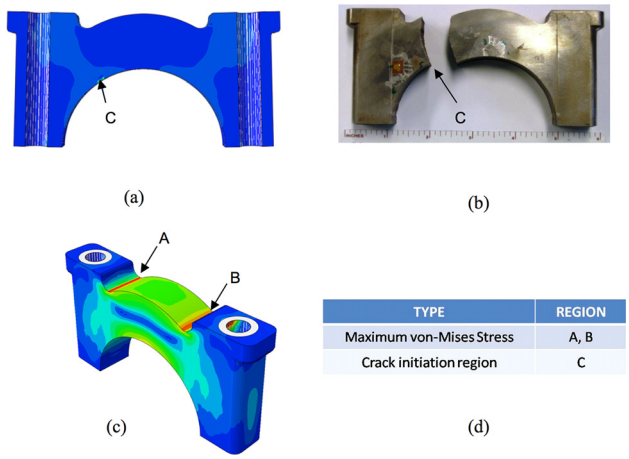

Fig. 16 Comparison of (*a*) finite element model with (*b*) experimental results indicating crack initiation at point C and (*c*) the regions of maximum Von Mises stress with the (*d*) tabulated results

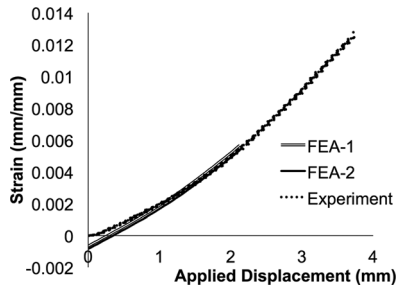

Fig. 17 Comparison of the experimental data with the finite element model at two different locations of the main bearing cap (where the strain gage was located)

5 Conclusions

An ISV constitutive model previously developed for wrought and cast materials was used (Ref. [8]) to examine the microscale plasticity-damage model correlation with experimental monotonic tests on a commercially available powder metallurgy material (FC-0205). The addition of a new coalescence ISV equation to the existing model allowed for accurate calibration of the model using experimental tension, compression, and torsion tests that allowed for material characterization of the material. Calibration of tension and compression experiments were completed at temperatures of 293 K and 573 K, while torsion calibration was limited to 293 K. Calibration of the model was also performed by using high rate Hopkinson/Kolsky compression data at 293 K. Validation of the model was then accomplished using notched tensile specimens with different triaxiality levels and monotonic testing of PM components. The model validation analysis produced load–displacement curves that compared well to the experimental results. The mechanical behavior was satisfactorily predicted for the quasi-static loading conditions even though certain discrepancies were observed in the results related to experimental uncertainties and model approximations.

Acknowledgment

This research was funded by U.S. Automotive Materials Partnership (AMD410) contract no. FC-26-02OR22910 with guidance from Howard I. Sanderow (Center for Powder Metallurgy Technology—CPMT), Russell A. Chernenkoff (Metaldyne), Paulo

Downloaded From: http://materialstechnology.asmedigitalcollection.asme.org/ on 09/25/2013 Terms of Use: http://asme.org/terms

Rosa (DaimlerChrysler), Shekhar G. Wakade (GM Powertrain), and Glen Weber (Ford Motor Company). We would also like to acknowledge the Center for Advanced Vehicular Systems (CAVS) at Mississippi State University for supporting this work.

Nomenclature

a = constant for nucleation equation
b = constant for nucleation equation
c = coalescence
c_2 = constant for nucleation equation
C_{TC} = temperature constant for coalescence equation
$C_{T\eta}$ = constant for nucleation equation
d = average inclusion particle size
d_g = average inclusion particle size
d_0 = pore diameter
$\underline{D}$ = rate of deformation
$\underline{D}^e$ = elastic rate of deformation
$\underline{D}^{in}$ = inelastic rate of deformation
$\underline{D}^p_d$ = isochoric inelastic rate of deformation
$\underline{D}^p_v$ = volumetric inelastic rate of deformation
f = initial particle volume fraction
F = deformation gradient
f(T) = rate sensitivity of yield
$\underline{F}^e$ = elastic portion of deformation gradient
$\underline{F}^p$ = inelastic portion of deformation gradient
$\underline{F}^p_d$ = isochoric inelastic portion of deformation gradient
$\underline{F}^p_v$ = volumetric inelastic portion of deformation gradient
G = Shear modulus
h = kinematic hardening modulus
H = isotropic hardening modulus
I_1 = first stress invariant
J = Jacobian
J_2 = second deviatoric stress invariant
J_3 = third deviatoric stress invariant
K_{IC} = fracture toughness
m = strain rate sensitivity parameter
n = strain hardening exponent
NND = pore nearest neighbor distance
R = isotropic hardening
r_d = kinematic dynamic recovery
r_s = kinematic static recovery
R_0 = initial pore radius
t = time
T = temperature
V = volume
V(T) = strain rate dependence on yield
Y(T) = rate independent yield
α = kinematic hardening
ζ = constant for coalescence equation
ε = strain
η = pore nucleation
λ, μ = elastic Lame constants
ν = pore growth
ρ = density
σ = stress
σ_e = equivalent Von Mises stress
σ_h = hydrostatic stress
φ = damage or volume fraction of pores

Appendix A

Horstemeyer et al. [8] modified the ISV plasticity model (Bammann et al. [5]) to account for stress state dependent damage evolution and to include the heterogeneities of microstructure for damage progression and failure analysis. Here the grain size, particle size, particle volume fraction, pore size, pore volume fraction, and pore nearest neighbor distances were required within the modeling framework. The pertinent equations in this model are denoted by the rate of change of the observable and internal state variables. The equations used within the context of the finite element method are given by

$$\overset{\circ}{\underline{\sigma}} = \dot{\underline{\sigma}} - \underline{W}^e\underline{\sigma} - \underline{\sigma}\underline{W}^e = \lambda(1-\phi_{total})tr(\underline{D}^e)\underline{I} + 2\mu(1-\phi_{total})\underline{D}^e - \frac{\dot{\phi}_{total}}{1-\phi_{total}}\underline{\sigma} \quad (A1)$$

$$\underline{D}^e = \underline{D} - \underline{D}^{in} \quad (A2)$$

$$\underline{D}^{in} = f(T)\sinh\left[\frac{\|\underline{\sigma}' - \underline{\alpha}\| - (R + Y(T))(1-\phi_{total})}{V(T)(1-\phi_{total})}\right]\frac{\underline{\sigma}' - \underline{\alpha}}{\|\underline{\sigma}' - \underline{\alpha}\|} \quad (A3)$$

$$\overset{o}{\underline{\alpha}} = \dot{\underline{\alpha}} - \underline{W}^e\underline{\alpha} + \underline{\alpha}\underline{W}^e = \left\{h(T)\underline{D}^{in} - \left[\sqrt{\frac{2}{3}}r_d(T)\|\underline{D}^{in}\| + r_s(T)\right]\|\underline{\alpha}\|\underline{\alpha}\right\}\left[\frac{d_{g0}}{d_g}\right]^z \quad (A4)$$

$$\dot{R} = \left\{H(T)\underline{D}^{in} - \left[\sqrt{\frac{2}{3}}R_d(T)\|\underline{D}^{in}\| + R_s(T)\right]R^2\right\}\left[\frac{d_{g0}}{d_g}\right]^z \quad (A5)$$

$$\dot{\phi}_{total} = \left[\dot{\phi}_{particles} + \dot{\phi}_{pores}\right]c + \left[\phi_{particles} + \phi_{pores}\right]\dot{c} \quad (A6)$$

$$\dot{\phi}_{particles} = \dot{\eta}v + \eta\dot{v} \quad (A7)$$

$$\dot{\eta} = \dot{\varepsilon}\frac{d^{1/2}}{K_{IC}f^{1/2}}\eta\left\{a\left[\frac{4}{27} - \frac{J_3^2}{J_2^3}\right] + b\frac{J_3}{J_2^{3/2}} + c\left\|\frac{I_1}{\sqrt{J_2}}\right\|\right\}\exp\left(-(C_{\eta T}/T)\right) \quad (A8)$$

$$\dot{\nu} = \frac{4}{3}\left[R_0\exp\left(\dot{\varepsilon}\frac{\sqrt{3}}{2(1-n)}\right)\sinh\left(\sqrt{3}(1-n)\frac{\sqrt{2}I_1}{3\sqrt{J_2}}\right)\right]^3 \quad (A9)$$

$$\dot{C} = \left(\frac{4d_0}{NND}\right)^{\zeta}\exp(C_{TC}T)\dot{\varepsilon} \quad (A10)$$

$$\dot{\phi}_{pores} = \left[\frac{1}{(1-\phi_{pores})^m} - (1-\phi_{pores})\right] \times \sinh\left\{\frac{2(2(V(T)/Y(T)) - 1)}{(2(V(T)/Y(T)) + 1)}\frac{\sigma_H}{\sigma_{vm}}\right\}\|\underline{\dot{\varepsilon}}\| \quad (A11)$$

The rate equations are generally written as objective rates ($\overset{o}{\underline{\sigma}}, \overset{o}{\underline{\alpha}}$) with indifference to the continuum frame of reference assuming a Jaumann rate in which the continuum spin equals the elastic spin ($\underline{W} = \underline{W}^e$). The ISV Eqs. (A4)–(A11) are functions of the observable variables (temperature, stress state, and rate of deformation). In general, the rate equations of generalized displacements, or thermodynamics fluxes, describing the rate of change may be written as independent equations for each ISV or as derivatives of a suitably chosen potential function arising from the hypothesis of generalized normality. An advantage of assuming generalized normality, although somewhat restrictive, is unconditional satisfaction of the Kelvin inequality of the second law of thermodynamics (nonnegative intrinsic dissipation), i.e.,

$$\underline{\sigma} : \underline{D}^{in} - \underline{b} : \overset{\circ}{\underline{\alpha}} - \kappa\cdot\dot{R} - Y_\eta\cdot\dot{\eta} - Y_v\cdot\dot{v} - Y_c\cdot\dot{c} \geq 0 \quad (A12)$$

The selection of the ISVs may, in principle, be somewhat arbitrary, but the kinematic hardening, isotropic hardening, and damage rate equations are physically motivated and strongly influence the history of the material. The ISV model accounts for deviatoric inelastic deformation resulting from the presence of dislocations in crystallographic material, dilatational deformation, and ensuing failure from damage progression.

Downloaded From: http://materialstechnology.asmedigitalcollection.asme.org/ on 09/25/2013 Terms of Use: http://asme.org/terms

The elastic Lame constants are denoted by λ and μ. The elastic rate of deformation ($\underline{D}^e$) results when the flow rule as shown in Eq. (A3) is subtracted from the total deformation ($\underline{D}$), which is defined by the boundary conditions that comes from the finite element analysis. The independent variables for the inelastic rate of deformation are given as the stress, temperature, and internal state variables. This is similar to power law and Garofalo [13] equations for creep except that the ISVs are now included. The deviatoric inelastic flow rule, $\underline{D}^{in}$, encompasses the regimes of creep and plasticity and is a function of the temperature, the kinematic hardening internal state variable ($\underline{\alpha}$), the isotropic hardening internal state variable (R), the volume fraction of damaged material (ϕ), and the functions $f(T)$, $V(T)$, and $Y(T)$, which are related to yielding with Arrhenius-type temperature dependence. The function $Y(T)$ is the rate-independent yield stress. The function $f(T)$ determines when the rate-dependence affects initial yielding. The function $V(T)$ determines the magnitude of rate-dependence on yielding. These functions are determined from simple isothermal compression tests with different strain rates and temperatures,

$$V(T) = C_1 \exp(-C_2/T), \quad Y(T) = C_3 \exp(C_4/T), \quad f(T) = C_5 \exp(-C_6/T) \tag{A13}$$

The kinematic hardening internal state variable, $\underline{\alpha}$, reflects the effect of anisotropic dislocation density, and the isotropic hardening internal state variable R, reflects the effect of the global dislocation density. As such, the hardening Eqs. (A4)–(A5) are cast in a hardening-recovery format that includes dynamic and static recovery. The functions $r_s(T)$ and $R_s(T)$ are scalar in nature and describe the diffusion-controlled static or thermal recovery, while $r_d(T)$ and $R_d(T)$ are scalar functions describing dynamic recovery. Hence, the two main types of recovery that are exhibited by populations of dislocations within crystallographic materials are captured in the ISVs. The anisotropic hardening modulus is $h(T)$, and the isotropic hardening modulus is $H(T)$. The hardening moduli and dynamic recovery functions account for deformation-induced anisotropy arising from texture and dislocation substructures by means of stress-dependent variables. By using J_3' in the hardening equations the different hardening rates between axisymmetric compression and torsion (torsional softening) were accurately captured

$$r_d(T) = C_7\left(1 + C_{19}\left[\frac{4}{27} - \frac{J_3'^2}{J_2'^3}\right]\right)\exp(-C_8/T) \tag{A14}$$

$$h(T) = \left\{C_9\left(1 + C_{20}\left[\frac{4}{27} - \frac{J_3'^2}{J_2'^3}\right]\right)\right\} - C_{10}T \tag{A15}$$

$$r_s(T) = C_{11}\exp(-C_{12}/T) \tag{A16}$$

$$R_d(T) = C_{13}\left(1 + C_{21}\left[\frac{4}{27} - \frac{J_3'^2}{J_2'^3}\right]\right)\exp(-C_{14}/T) \tag{A17}$$

$$H = \left\{C_{15}\left(1 + C_{22}\left[\frac{4}{27} - \frac{J_3'^2}{J_2'^3}\right]\right)\right\} - C_{16}T \tag{A18}$$

$$R_s(T) = C_{17}\exp(-C_{18}/T) \tag{A19}$$

where $J_2' = \frac{1}{2}(\underline{\sigma}' - \underline{\alpha})^2$ and $J_3' = \frac{1}{3}(\underline{\sigma}' - \underline{\alpha})^3$. The deviatoric stress $\underline{\sigma}'$ is expressed in indicial notation as

$$\sigma_{ij}' = \sigma_{ij} - \frac{1}{3}\sigma_{ii} \tag{A20}$$

The damage variable ϕ represents the damaged fraction of material within a continuum element. The damage reduces the material strength, enhance the inelastic flow, and soften the elastic moduli in the region where it is growing. Equations (A7)–(A11) introduces the void volume fraction (porosity) as damage. By including damage, ϕ, as an ISV, different forms of damage rules can easily be incorporated into the constitutive framework. Bammann and Aifantis [11] demonstrated the applicability of the Cocks and Ashby [17] void growth rule used as the damage rate equation in the ISV model. In the framework above, each damage component (nucleation, η, growth, v, and coalescence, c) evolve as ISVs.

The generalized thermodynamic force conjugate, Y, is often referred to as the energy release rate for elastic brittle materials and the J-integral for inelasticity. In essence, an increment of damage will have associated energy released per unit damage extension as new damaged area (or volume) is developed.

The damage progression is divided into void nucleation and growth from second phase particles and from pores. Coalescence ISV in Eq. (A10) is introduced to reflect pore–pore interactions and particle-pore interactions. The void nucleation ISV in Eq. (A8) is discussed in length by Horstemeyer and Gokhale [7]. The void growth ISV related to particles inducing pores/voids, Eq. (A9). Other forms can be used and evaluated, but this equation allows for a strain rate sensitivity in relation the plasticity model ($m = V(T)/Y(T)$). For the porosity evolution, the Cocks and Ashby [10] void growth rule is used as shown in Eq. (A11). In these equations, the microstructural features to be used are the following: particle size, d, volume fraction of particles, f, grain size, d_g, pore size, p, $v_{initial} = 4/3\pi(p/2)^3$, volume fraction of pores, ϕ_{pores}.

Appendix B: Microstructure-Property (Elastic–Plastic) Model Constants for FC-0205

		Constants
Material property information	G (MPa)	80,384
	a	0
	Bulk (MPa)	174,167
	b	0
	Melting temp (K)	1811
Yield stress and adjustment constants (Eq. (A13))	C1 (MPa)	20
	C2 (K)	0
	C3 (MPa)	376
	C4 (K)	0
	C5 (1/MPa)	1×10^{-5}
	C6 (K)	0
Kinematic hardening and recovery terms (Eqs. (A14)–(A16))	C7 (1/MPa)	1.5
	C8 (K)	87.5
	C9 (MPa)	59,000
	C10 (K)	0.75
	C11 (s/MPa)	0
	C12 (K)	0
Isotropic hardening and recovery terms (Eqs. (A17)–(A19))	C13 (1/MPa)	0.01
	C14 (K)	14
	C15 (MPa)	7800
	C16 (K)	0.04
	C17 (s/MPa)	0
	C18 (K)	0
Hardening and recover cons	Ca	−9.1
	Cb	−0.35
Temperature	Init. temp (K)	293
	Heat gen. coeff	0.34

Downloaded From: http://materialstechnology.asmedigitalcollection.asme.org/ on 09/25/2013 Terms of Use: http://asme.org/terms

Appendix C: Microstructure-Property (Damage) Model Constants for FC-0205

	Constants	
McClintock pore growth (Eq. (A9))	Pore growth exp	0.3
	Init. radius (mm)	0.0055
Nucleation (Eq. (A8))	A	1
	B	1
	C	1
	Nuc coeff	2×10^{-006}
	Fract. toughness MPa (m 1/2)	40
	Part. size (mm)	0
	Part. vol fract.	0
Coalescence (Eq. (A5))	cd1	1
	cd2	1
	gs0 (μm)	15
	gs (μm)	15
	gs exp. Zz	0.3
	Init. pore vol. fract.	0.19
CA pore growth (Eq. (A11))	Pore growth constant	16
Nucleation (Eq. (A8))	Nuc. temp. depend.	0
Coalescence (Eq. (A10))	Coal. temp. depend.	0
Yield strength adjustment terms (Eqs. (A14)–(A15))	c19	0
	c20	0
Modulus-porosity adjustment term (Eq. (A10))	ζ	3

References

[1] Hammi, Y., Stone, T. Y., and Horstemeyer, M. F., 2005, "Constitutive Modeling of Metal Powder Behavior During Compaction," SAE Technical Paper No. 2005-01-0632.

[2] Davison, L., Stevens, A. L., and Kipp, M. E., 1977, "Theory of Spall Damage Accumulation in Ductile Metals," J. Mech. Phys. Solids, **25**(1), pp. 11–28.

[3] Gurson, A. L., 1977, "Continuum Theory of Ductile Rupture by Void Nucleation and Growth: Part I—Yield Criteria and Flow Rules for Porous Ductile Media," ASME J. Eng. Mater. Technol., **99**(1), pp. 2–15.

[4] Gurson, A. L., 1977, "Porous Rigid-Plastic Materials Containing Rigid Inclusions-Yield Function, Plastic Potential, and Void Nucleation," Proceedings of the Fourth International Conference on Fracture (ICF4), Waterloo, Canada, June 19, Vol. 2A, D. M. R. Taplin, ed., University of Waterloo Press, Waterloo, ON, Canada, pp. 357–364.

[5] Leblond, J. B., Perrin, G., and Devaux, J., 1995, "An Improved Gurson-Type Model for Hardenable Ductile Metals," Eur. J. Mech. A/Solids, **14**(4), pp. 499–527.

[6] Tvergaard, V., 1989, "Material Failure by Void Growth to Coalescence," Adv. Appl. Mech., **27**(1), pp. 83–151.

[7] Marin, E. B., and Mcdowell, D. L., 1996, "Associative Versus Non-Associative Porous Viscoplasticity Based on Internal State Variable Concepts," Int. J. Plast., 12(5), pp. 629–669.

[8] Horstemeyer, M. F., Lathrop, J., Gokhale, A. M., and Dighe, M., 2000, "Modeling Stress State Dependent Damage Evolution in a Cast Al-Si-Mg Aluminum Alloy," Theor. Appl. Fract. Mech., **33**(1), pp. 31–47.

[9] Mähler, L., Ekh, M., and Runesson, K., 2001, "A Class of Thermo-Hyperelastic-Viscoplastic Models for Porous Materials: Theory and Numerics," Int. J. Plast., 17(7), pp. 943–969.

[10] Bammann, D. J., 1984, "An Internal Variable Model of Viscoplasticity," Int. J. Eng. Sci., **22**(8–10), pp. 1041–1053.

[11] Bammann, D. J., and Aifantis, E. C., 1989, "A Damage Model for Ductile Metals," Nucl. Eng. Des., **116**(3), pp. 355–362.

[12] Bammann, D. J., 1990, "Modeling Temperature and Strain Rate Dependent Large Deformations of Metals," ASME Appl. Mech. Rev., **43** 5(Part 2), pp. 312–319.

[13] Bammann, D. J., Chiesa, M. L., Horstemeyer, M. F., and Weingarten, L. I., 1993, "Failure in Ductile Materials Using Finite Element Methods," *Structural Crashworthiness and Failure*, N. Jones and T. Wierzbicki, eds., Elsevier, Amsterdam.

[14] Bammann, D. J., Chiesa, M. L., and Johnson, G. C., 1996, "Modeling Large Deformation and Failure in Manufacturing Processes," *Theoretical and Applied Mechanics*, T. Tatsumi, E. Wannabe, and T. Kambe, eds., Elsevier, Amsterdam, pp. 359–376.

[15] Horstemeyer, M. F., and Gokhale, A. M., 1999, "A Void-Crack Nucleation Model for Ductile Metals," Int. J. Solids Struct., **36**(33), pp. 5029–5055.

[16] McClintock, F. A., 1968, "A Criterion for Ductile Fracture by Void Growth of Holes," ASME J. Appl. Mech., **35**(1), pp. 363–371.

[17] Cocks, A. C. F., and Ashby, M. F., 1982, "On Creep Fracture by Void Growth," Prog. Mater. Sci., **27**(3–4), pp. 189–244.

[18] Lee, E. H., 1969, "Elastic-Plastic Deformation at Finite Strain," ASME J. Appl. Mech., **36**(1), pp. 1–6.

[19] Horstemeyer, M. F., 2001, "From Atoms to Autos: A New Design Paradigm Using Microstructure-Property Modeling. Part 1: Monotonic Loading Conditions," Sandia National Laboratory, Livermore, CA, Technical Report No. SAND2000-8662.

[20] Horstemeyer, M. F., Matalanis, M. M., Sieber, A. M., and Botos, M. L., 2000, "Micromechanical Finite Element Calculations of Temperature and Void Configuration Effects on Void Growth and Coalescence," Int. J. Plast., **16**(7–8), pp. 979–1015.

[21] Metaldyne, 2007, "Fc-0205 Powder Metal Production," http://metaldyne.com

[22] ASTM Standard E8, 2009, "Standard Test Methods for Tension Testing of Metallic Materials," ASTM International, West Conshohocken, PA.

[23] Allison, P. G., Horstemeyer, M. F., Hammi, Y., Brown, H. R., Tucker, M. T., and Hwang, Y.-K., 2011, "Microstructure-Property Relations of a Powder Metallurgy Steel (Fc-0205) Under Varying Temperatures, Strain Rates, and Stress States," Mater. Sci. Eng., A, **529**(25), pp. 335–344.

[24] German, R. M., 2005, *Powder Metallurgy and Particulate Materials Processing*, MPIF, Princeton, NJ.

[25] Bridgman, P. W., 1923, "The Compressibility of Thirty Metals as a Function of Pressure and Temperature," Proc. Am. Acad. Arts Sci., **58**(5), pp. 165–242.

Downloaded From: http://materialstechnology.asmedigitalcollection.asme.org/ on 09/25/2013 Terms of Use: http://asme.org/terms